J Neuropathol Exp Neurol

Vol. 68, No. 2
February 2009
pp. 125–135

ORIGINAL ARTICLE

Neuropathology of the *Mcoln1*$^{-/-}$ Knockout Mouse Model of Mucolipidosis Type IV

Matthew C. Micsenyi, MS, Kostantin Dobrenis, PhD, Gloria Stephney, MS, James Pickel, PhD, Marie T. Vanier, MD, PhD, Susan A. Slaugenhaupt, PhD, and Steven U. Walkley, DVM, PhD

Abstract

The recently developed *Mcoln1*$^{-/-}$ knockout mouse provides a novel model for analyzing mucolipin 1 function and mucolipidosis type IV disease. Here we characterize the neuropathology of *Mcoln1*$^{-/-}$ mouse at the end stage. Evidence of ganglioside accumulation, including increases in GM2, GM3, and GD3 and redistribution of GM1, was found throughout the central nervous system (CNS) independent of significant cholesterol accumulation. Unexpectedly, colocalization studies using immunofluorescence confocal microscopy revealed that GM1 and GM2 were present in separate vesicles within individual neurons. While GM2 was significantly colocalized with LAMP2, consistent with late-endosomal/lysosomal processing, some GM2-immunoreactivity occurred in LAMP2-negative sites, suggesting involvement of other vesicular systems. P62/Sequestosome 1 (P62/SQSTM1) inclusions were also identified in the CNS of the *Mcoln1*$^{-/-}$ mouse, suggesting deficiencies in protein degradation. Glial cell activation was increased in brain, and there was evidence of reduced myelination in cerebral and cerebellar white matter tracts. Autofluorescent material accumulated throughout the brains of the knockout mice. Finally, axonal spheroids were prevalent in white matter tracts and Purkinje cell axons. This neuropathological characterization of the *Mcoln1*$^{-/-}$ mouse provides an important step in understanding how mucolipin 1 loss of function affects the CNS and contributes to mucolipidosis type IV disease.

Key Words: Axonal spheroids, Bis(monoacylglycero) phosphate, Gangliosides, Lysosomal disease, Mucolipin 1, P62/Sequestosome 1.

INTRODUCTION

Mucolipidosis type IV (MLIV) is an autosomal recessive lysosomal disease caused by mutations in the *MCOLN1* gene encoding the late-endosomal/lysosomal transient receptor potential channel, mucolipin 1 (TRP-ML1) (1–3). Clinically, MLIV presents as a complex disease with manifestations that include developmental delays, impaired gastric function, mental retardation, motor deficits, and ophthalmologic abnormalities (4–7). The major pathologic finding in MLIV disease patients is the accumulation of granulomembranous storage bodies in all cells. This storage material contains lipids such as sphingolipids (specifically gangliosides), phospholipids, and cholesterol, along with acid-mucopolysaccharides (8–11).

The function of TRP-ML1 and the mechanisms by which loss of function mutations in the protein result in storage remain unknown. Evidence has suggested that normal TRP-ML1 functions as a nonselective cation channel and that channel activity is regulated in a pH- and Ca^{2+}-dependent manner (12, 13).

Studies of MLIV disease have observed that TRP-ML1 mediates lipid trafficking by regulating late-endosomal/lysosomal fission and fusion events (14–17). Therefore, it is believed that endocytosed material is inefficiently trafficked or is mistrafficked, thereby accumulating as intracytoplasmic membranous inclusions rather than being properly targeted to lysosomes in which the material may be degraded.

In contrast, there is some evidence suggesting that MLIV disease is a metabolic disorder rather than a trafficking disorder. Mucolipin 1 may act as an H^+ transporter in late endosomes/lysosomes, thereby playing a role in regulating luminal pH of these compartments and ultimately hydrolase activity (18–20). In TRP-ML1–deficient cells (including MLIV patient fibroblasts and cultured cells targeted with small interfering RNA to TRP-ML1), lysosomal pH has been shown to be altered, and this presumably leads to lysosomal dysfunction (18–20).

Recently, the novel *Mcoln1*$^{-/-}$ knockout mouse has been developed as a model of human MLIV disease. Neuropathological findings include an increase in the presence of LAMP2-positive vesicles primarily in neurons throughout the central nervous system (CNS) (21). In addition, by electron microscopy (EM), storage bodies that ultrastructurally resemble the inclusions found in human MLIV disease have been found to accumulate in perinuclear regions of neuronal perikaryon (21).

The purpose of the current study was to characterize the neuropathological consequences of TRP-ML1 loss of function in the *Mcoln1*$^{-/-}$ mouse at the end stage (i.e. at 8 months of age). We identified ganglioside accumulation, the presence of P62/Sequestosome 1 (SQSTM1) inclusions,

From the Dominick P. Purpura Department of Neuroscience (MCM, KD, GS, SUW), Rose F. Kennedy Center for Research in Mental Retardation and Human Development, Albert Einstein College of Medicine, Bronx, New York; National Institute of Mental Health (JP), National Institutes of Health, Bethesda, Maryland; Institut National de la Santé et de la Recherche Médicale (MTV), Laënnec Medical School and Lyon University, Lyon, France; and Center for Human Genetic Research (SAS), Massachusetts General Hospital and Harvard Medical School, Boston, Massachusetts.

Send correspondence and reprint requests to: Steven U. Walkley, DVM, PhD, Dominick P. Purpura Department of Neuroscience, Albert Einstein College of Medicine, 1410 Pelham Parkway South, Room 618, Bronx, NY 10461; E-mail: walkley@aecom.yu.edu

These studies were supported by Grant No. NIH RO1 HD045561 (SUW) and NIH R01 NS39995 (SAS) from the National Institutes of Health.

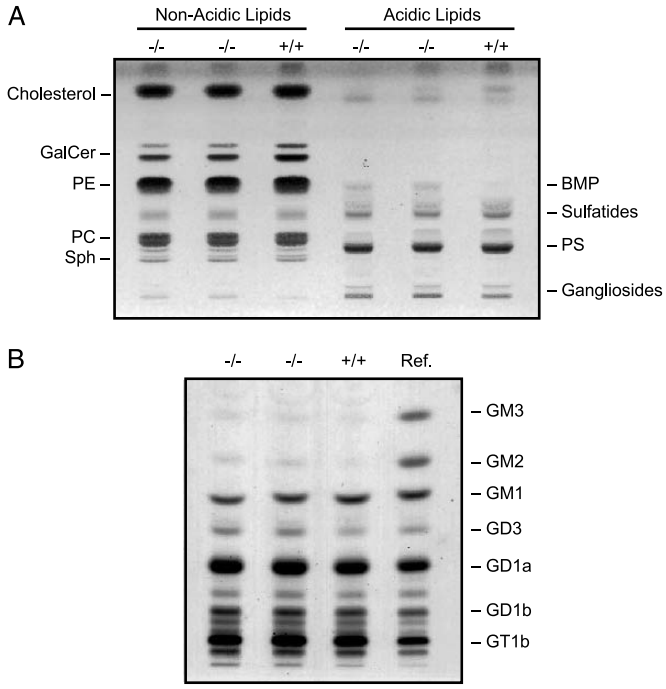

FIGURE 1. Biochemical analysis of lipid profiles in cerebrum of end-stage (8-month-old) *Mcoln1*$^{-/-}$ mice. **(A)** Nonacidic and acidic lipid fractions of cerebrum from *Mcoln1*$^{-/-}$ mice (−/−) and wild-type (Wt) control mice (+/+). GalCer, galactosylceramide; PE, ethanolamine phosphoglycerides; PC, choline phosphoglycerides; Sph, sphingomyelin; BMP, bis(monoacylglycero)phosphate; PS, serine phosphoglycerides. **(B)** Ganglioside profiles of *Mcoln1*$^{-/-}$ (−/−), Wt control mice (+/+), and a reference Niemann-Pick C1 mouse.

glial cell activation and reduced myelination, the presence of autofluorescent material, and the formation of axonal spheroids in the brains of *Mcoln1*$^{-/-}$ mice.

MATERIALS AND METHODS

Animals and Tissue Collection

Mcoln1$^{-/-}$ knockout mice on a C57BL6 × 129S6 mixed background were genotyped as described previously by polymerase chain reaction (21). Wild-type littermate mice were used as controls in all experiments. Niemann-Pick type C1 (NPC1) mice (BALBc/*NPC*^{nih} mice) were originally obtained from Peter Pentchev at the National Institutes of Health (Bethesda, MD). Mice were deeply anesthetized at end stage (i.e. 8 months of age) with sodium pentobarbital (150 mg/kg) and perfused transcardially with 0.9% saline followed by excision of the right cerebral hemisphere, which was immediately frozen for biochemical analysis. Transcardial fixation perfusion was then performed using 4.0% paraformaldehyde in 0.1 M phosphate buffer, as described previously (21). The remaining cerebral and cerebellar tissue was excised and immersion fixed overnight before being transferred to 0.1 M phosphate buffer for storage at 4°C. All procedures using animals were approved by the Institutional Animal Care and Use Committee of the Albert Einstein College of Medicine.

Antibodies and Reagents

Anti-GM1 ganglioside rabbit polyclonal antibody (pAb) (whole serum; cat. #G2006-11) was purchased from US Biologicals (Swampscott, MA). Anti-GM2 ganglioside mouse monoclonal antibody (mAb) was produced in-house as a supernatant from hybridoma clone 10-11 cells kindly provided by Progenics Pharmaceuticals, Inc (Tarrytown, NY). Anti-GM3 ganglioside mouse mAb (hybridoma clone DH2; supernatant) was generously provided by Dr S. Hakomori (Pacific Northwest Research Laboratory, Seattle, WA). Anti-GD3 ganglioside mouse mAb (hybridoma clone R-24; supernatant; cat. #1977) was purchased from Matreya, LLC (Pleasant Gap, PA). The LAMP2 rat mAb (cat. #ABL-93-c) developed by J. T. August was obtained from the Developmental Studies Hybridoma Bank developed under the auspices of the National Institute of Child Health and Human Development (NICHD)

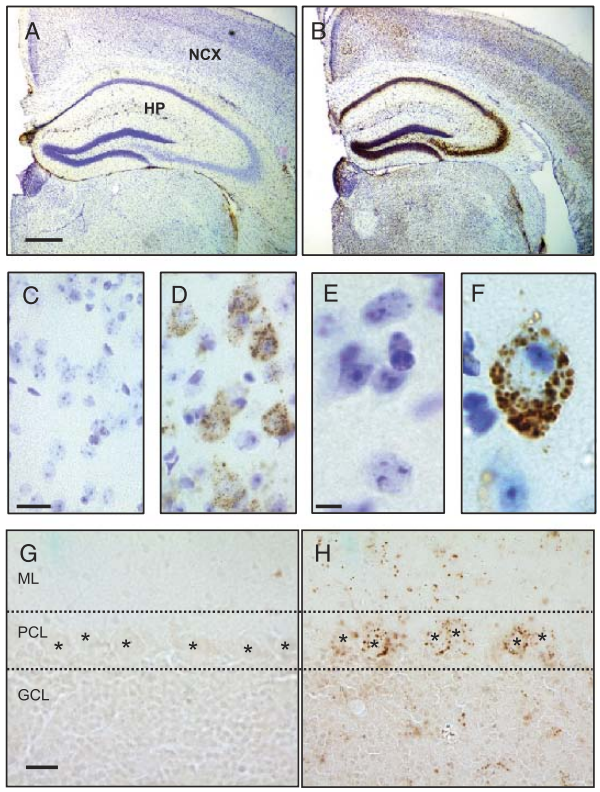

FIGURE 2. Accumulation of GM2 ganglioside in the CNS of the *Mcoln1*$^{-/-}$ mouse. **(A, B)** Hemicoronal brain sections stained for GM2 and counterstained with Nissl showing almost no positive immunoreactivity in a wild-type (Wt) mouse **(A)**, but strong staining throughout the neocortex (NCX) and hippocampus (HP) in the *Mcoln1*$^{-/-}$ mouse **(B)**. **(C–F)** Higher magnification of Wt **(C, E)** cortical sections and GM2 storage in pyramidal neurons (based on size and morphology) of the *Mcoln1*$^{-/-}$ mouse **(D, F)**. **(G, H)** In addition, cerebellar sections stained for GM2 ganglioside showed no accumulation in a Wt mouse **(G)**, but sporadic accumulation in a *Mcoln1*$^{-/-}$ mouse **(H)** including in Purkinje cells (denoted by *) of the Purkinje cell layer (PCL), the molecular layer (ML), and the granule cell layer (GCL). Scale bars = **(A)** 500 μm and also pertains to **B; (C)** 10 μm and pertains to **D**; **(E)** 5 μm and pertains to **F**; **(G)** 20 μm and pertains to **H**.

and maintained by The University of Iowa, Department of Biological Sciences, Iowa City, IA. Anti-P62/SQSTM1 rabbit pAb (whole serum; cat. #PW9860) was purchased from Biomol Int, LP (Exeter, UK). Anti-glial fibrillary acidic protein (GFAP) mouse mAb (hybridoma clone G-A-5; ascites; cat. #G3893) was purchased from Sigma-Aldrich (St Louis, MO). Anti-CD11b, a marker of microglia, was a rat mAb (hybridoma clone 5C6; affinity purified supernatant; cat. #MCA711) purchased from AbD Serotec (Oxford, UK). Anti-subunit C of mitochondrial ATP synthase (SCMAS) rabbit pAb was generously provided by Dr E. F. Neufeld (University of California, Los Angeles, Los Angeles, CA). Anti-calbindin D-28K rabbit pAb (affinity purified; cat. #AB1778) was purchased from Millipore (Billerica, MA) and mouse mAb (hybridoma clone CB-955; ascites; cat. #C9848) from Sigma-Aldrich. Nonspecific rabbit serum (R9133), mouse IgM (M2521), and IgG from rat serum (I4131) was purchased from Sigma-Aldrich. Secondary antibodies used for immunohistochemistry were biotinylated goat anti-mouse IgM (BA-2020), biotinylated goat anti-mouse IgG (BA-9200), biotinylated goat anti-rat IgG (BA-9400), and biotinylated goat anti-rabbit IgG (BA-1000) from Vector Laboratories (Burlingame, CA). Secondary antibodies used for immunofluorescence microscopy were Alexa Fluor 488 goat anti-rat

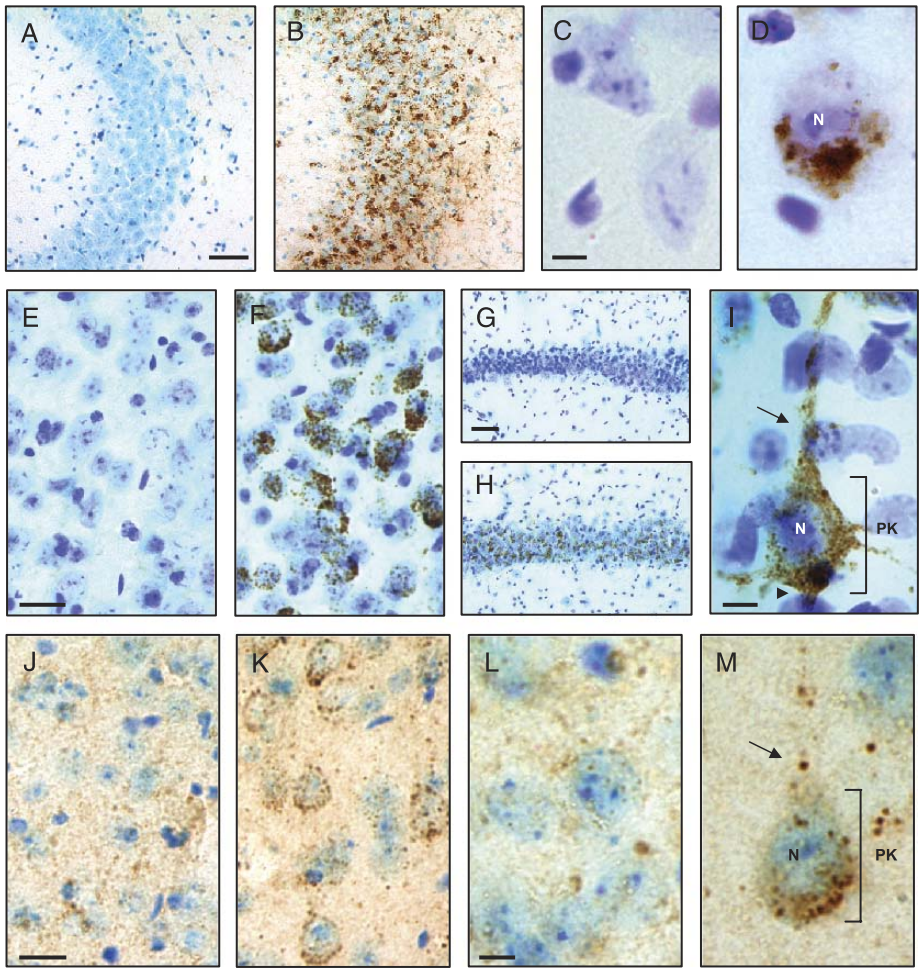

FIGURE 3. GM3, GD3, and GM1 ganglioside accumulation in cerebral brain tissue of the *Mcoln1*$^{-/-}$ mouse by immunohistochemistry. **(A, B)** Hemicoronal cerebral brain sections immunoperoxidase labeled for GM3 and Nissl counterstained showed no accumulation in the CA3 region of the hippocampus of a wild-type (Wt) mouse **(A)**, but significant accumulation in a *Mcoln1*$^{-/-}$ mouse **(B)**. **(C, D)** Similarly, high magnification images of cortical pyramidal neurons showed no GM3 in a Wt mouse **(C)**, but perinuclear accumulation of GM3 in neurons of the *Mcoln1*$^{-/-}$ mouse **(D)**. **(E–I)** Immunoperoxidase labeling for GD3 in the amygdala showed no accumulation in a Wt mouse **(E)** but significant accumulation in the *Mcoln1*$^{-/-}$ mouse **(F)**. GD3 accumulation was also absent in the CA1/CA2 region of the hippocampus of a Wt mouse **(G)** but is conspicuous throughout this region of a *Mcoln1*$^{-/-}$ mouse **(H)**. Cortical pyramidal neuron of the *Mcoln1*$^{-/-}$ mouse **(I)** showed large amounts of GD3 accumulation throughout the perikaryon as well as in the axon hillock, apical dendrite, and other neuritic processes. **(J–L)** GM1 ganglioside appeared redistributed in an intracellular vesicular pattern in cortical pyramidal neurons of the *Mcoln1*$^{-/-}$ mouse **(K, M)** compared with a Wt mouse **(J, M)** by immunoperoxidase labeling. Scale bars = **(A** and **G** 50 μm and also pertain to **B** and **H**, respectively; **(C** and **L)** 5 μm and pertain to **D** and **M**, respectively; **(E** and **J)** 10 μm and pertain to **F** and **K**, respectively; **(I)** 5 μm. Nucleus, N; axon hillock, arrowhead; perikaryon, PK; apical dendrite, arrow.

IgG (A-11006) and Alexa Fluor 546 goat anti-mouse IgM (A-21045) from Invitrogen (Carlsbad, CA). Fluorescein isothiocyanate goat anti-rabbit IgG (JGZ095144) was from Accurate Chemical & Scientific Corp. (Westbury, NY). Filipin complex from *Streptomyces filipinensis* (F9765) was used to detect nonesterified cholesterol and purchased from Sigma-Aldrich.

Biochemical Lipid Analysis

Total lipid extracts were obtained from frozen cerebrum collected after saline perfusion of mice using an exraction method that ensures optimal ganglioside recovery (22). Desalting and separation of total lipids into a neutral and an acidic fraction by reverse-phase chromatography on Bond-Elute C18 columns (Varian, Palo Alto, CA) and further analytical methods were similar to those used in a previous study (23). For general analysis of the main lipid classes, aliquots corresponding to 2 mg tissue were spotted on high-performance thin layer chromatographic (HPTLC) silica gel 60 plates (Merck, Darmstadt, Germany) developed in chloroform-methanol-water 65:25:4 (vol/vol/vol) and visualized by an anisaldehyde spray. The acidic lipid fraction from the Bond-Elute C18 columns was used without further purification for ganglioside analysis. Total sialic acid was measured by the Svennerholmn's resorcinol-HCl method (22). Aliquots corresponding to 3 mg tissue were spotted on HPTLC silica gel 60 plates using a Linomat 4 apparatus (Camag, Muttenz, Switzerland). The plates were developed in chloroform-methanol-0.2% $CaCl_2$ 55:45:10 (vol/vol/vol) and sprayed by the resorcinol-HCl spray (22). Quantitative evaluation was performed at 580 nm using a Camag TLC-Scanner II/Cats 3 software system (22). Tissue from an NPC1 mouse was used as a reference control in the HPTLC analysis. Concentrations of individual gangliosides were calculated from the percentage of each ganglioside and the total lipidic sialic acid values, taking into account the number of sialic acids for each ganglioside moiety.

Histochemistry

Hemicoronal cerebral and sagittal cerebellar brain sections, 35-μm-thick, were cut using a Leica VT-1000S vibratome; immunoperoxidase staining and filipin labeling of tissue were performed as previously described (24). Briefly, for immunoperoxidase, sections were blocked at room temperature (RT) for 1 hour in block solution (1% bovine serum albumin [BSA], 1.5% normal goat serum [NGS], and 0.02% saponin in phosphate-buffered saline [PBS]). Primary antibody incubation was performed overnight at 4°C in diluent (1% BSA, 1% NGS, and 0.02% saponin in PBS). Biotinylated secondary antibody in diluent was next applied to sections at RT for 1 hour, followed by incubation with Vectastain avidin and biotinylated horseradish peroxidase macromolecular complex (ABC) kit (Vector Laboratories PK-4000) for 1 hour at RT. Sections were then stained with 3,

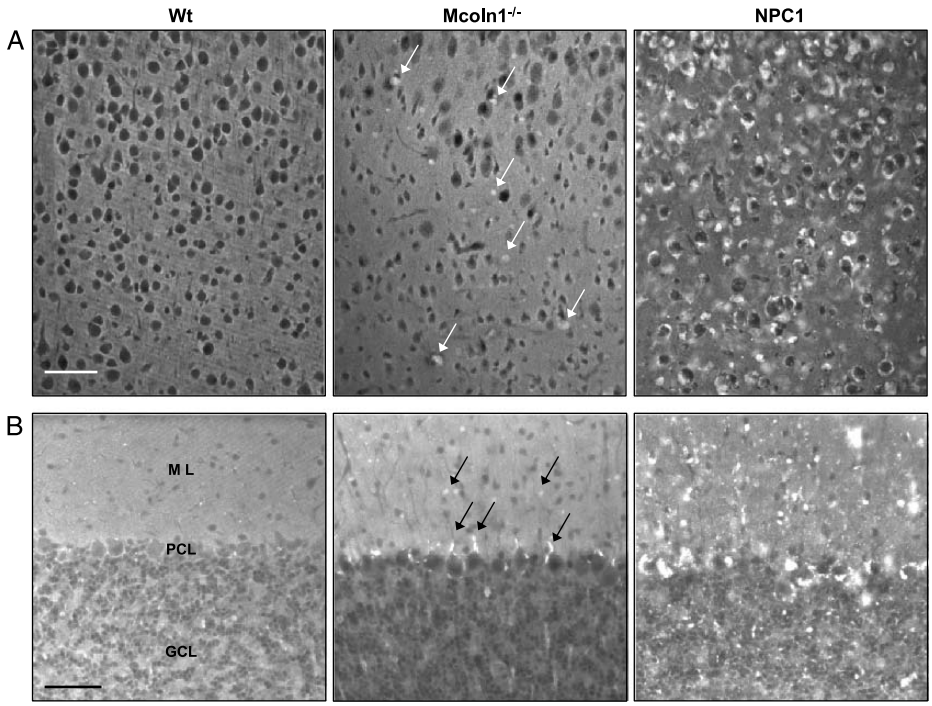

FIGURE 4. Cholesterol in the brain of the *Mcoln1*$^{-/-}$ mouse. **(A)** Cerebral cortical sections were labeled with filipin to detect nonesterified cholesterol accumulation. There was no significant labeling in a wild-type (Wt) mouse, but some focal accumulation in the *Mcoln1*$^{-/-}$ mouse (arrows). Niemann-Pick C1 (NPC1) mouse tissue was used as a reference. **(B)** Cerebellar sections labeled with filipin similarly show minimal cholesterol in the Wt mouse but occasional accumulation in the molecular cell layer and apical dendrites of Purkinje cells. The NPC1 mouse tissue shows abundant cholesterol accumulation. Arrows indicate filipin-positive cholesterol accumulation. ML, molecular layer; PCL, Purkinje cell layer; GCL, granule cell layer. Scale bars = **(A)** 50 μm and also pertains to the top 3 panels; **(B)** 50 μm and pertains to the bottom 3 panels.

3′-diaminobenzidine (DAB) substrate kit for peroxidase (Vector Laboratories SK-4100) and further counterstained with Nissl before mounting with Permount (Fisher SP15-500). For filipin labeling, a stock solution of filipin complex in dimethyl sulfoxide (25 mg/ml) was diluted 1:500 in PBS, and sections were incubated in this solution for 20 minutes at RT before being mounted with Prolong Antifade Kit from Invitrogen (P7841). As a negative control for immunoperoxidase staining runs, primary antibodies were omitted from tissue sections followed by incubation with appropriate secondary antibodies. Niemann-Pick type C1 tissue sections were used as a positive control in filipin labeling experiments. For Luxol fast blue staining, tissues were processed using an ASP300 automated processor, hand-embedded in paraffin blocks, and sectioned on a microtome at 5 μm. Sections were then stained for myelin by Luxol fast blue and counterstained with cresyl violet. Tissue sections were examined and photographed using an Olympus AX70 upright epifluorescence microscope equipped with MagnaFire CCD camera from Optronics (Goleta, CA).

Immunofluorescence and Confocal Fluorescence Microscopy

Tissue sections were cut and processed as described previously (24). Briefly, for immunofluorescence, 35-μm-thick sections were blocked (1% BSA, 10% NGS, and 0.02% saponin in PBS) at RT for 1.5 hours and next incubated in primary antibody in diluent (1% BSA, 5% NGS, and 0.02% saponin in PBS) overnight at 4°C. Secondary antibody incubation was for 1 hour at RT, and sections were mounted with Prolong Antifade reagent (Invitrogen). For autofluorescence evaluations, freshly cut sections were directly mounted without any processing. Negative controls for immunofluorescence included omission of or substitution of primary antibodies with matching nonimmune immunoglobulin fractions. Confocal fluorescence imaging of tissue was performed using a Zeiss Meta Duo V2 laser scanning confocal microscope. Immunofluorescence images were acquired with a 63× oil objective, whereas a 20× objective was used for autofluorescence imaging. Autofluorescence images were acquired using 488- and 543-nm laser lines consecutively and emission bandwidths of 511 to 576 nm and 580 to 700 nm, respectively. The 2 acquisition channels were combined to produce the images shown in results. These settings were selected after a full-spectrum scan to evaluate peaks of emission for the autofluorescent material. Images were analyzed using MetaMorph software from Molecular Devices (Downingtown, PA).

Electron Microscopy

Brain tissue for EM was prepared as previously described (21). After perfusion and fixation of tissue described above, blocks for EM were postfixed in 2.5% glutaraldehyde in 0.1 M cacodylate buffer. Tissue samples were then transferred to 2% osmium tetroxide, followed by dehydration in alcohol and plastic embedding in Epon. Sections were then

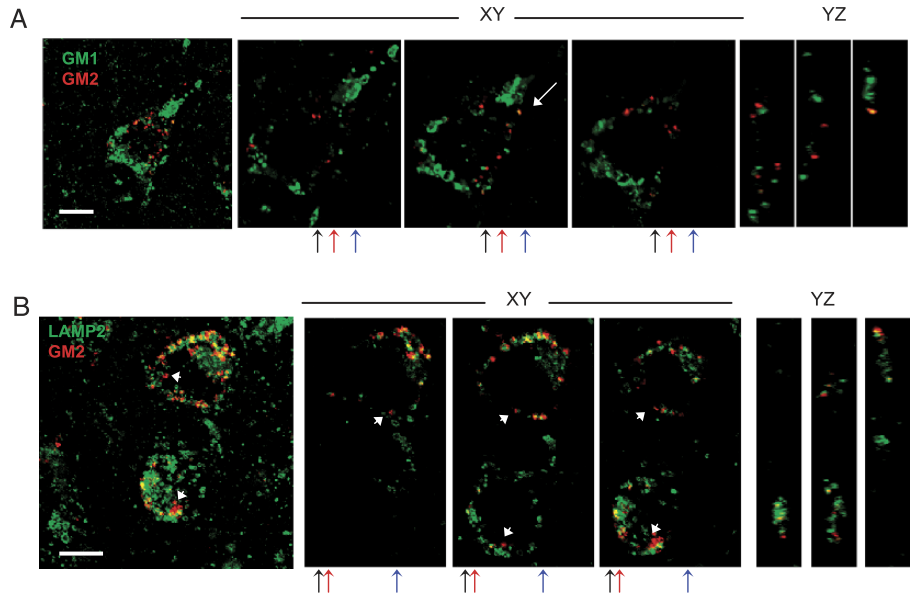

FIGURE 5. Colocalization of GM1 and GM2 gangliosides, and GM2 and LAMP2 in cortical pyramidal neurons of the *Mcoln1*$^{-/-}$ mouse by confocal microscopy. **(A)** Cerebral cortical sections labeled for GM1 (green) and GM2 gangliosides (red) show almost no colocalization (white arrow indicates colocalization). **(B)** Immunofluorescence labeling for LAMP2 (green) and GM2 ganglioside (red) shows colocalization in cortical pyramidal neurons of the *Mcoln1*$^{-/-}$ mouse (small white arrows indicate GM2 independent of LAMP2 and not colocalized). The first (left-most) image in **A** and **B** shows maximum projections of confocal z-series, followed by 3 single XY optical plane images taken at varying intervals along the *z* axis, and finally 3 single YZ orthogonal optical plane images at varying intervals. The XY images in **A** are a 2× magnification of the maximum projection image; the XY images in **B** are a 1.5× magnification of the corresponding maximum projection image. Black, red, and blue arrows indicate *y* axis at which orthogonal planes were sampled and correspond to the first, second, and third YZ images, respectively, from left to right. Scale bars = **(A** and **B)** 10 μm.

cut using an ultramicrotome and stained with uranyl acetate and lead citrate. Electron microscopy was performed using a Philips CM10 electron microscope.

RESULTS

Lipid Profiles of the *Mcoln1*$^{-/-}$ Mouse

The general lipid profiles of cerebra of end-stage *Mcoln1*$^{-/-}$ mice were compared with littermate wild-type (Wt) controls by HPTLC analysis. There was no apparent change in total cholesterol levels in the *Mcoln1*$^{-/-}$ mice. There was, however, a slight decrease in the level of galactosylceramide, the most specific myelin-associated lipid, in knockout compared with Wt mice (Fig. 1A). In addition, in the acidic-lipid fraction, there was an increase detected in a lipid identified as bis(monoacylglycero)phosphate (BMP), a phospholipid found in multivesicular late-endosomal and lysosomal internal membranes (Fig. 1A) (25). Visual examination of the HPTLC ganglioside profiles of cerebrum in the end-stage *Mcoln1*$^{-/-}$ mouse indicated no major change. However, there was a small but significant increase in the proportions of both GM2 and GM3 (Fig. 1B). A brain ganglioside extract from a mouse model of NPC1 disease (which is well documented as having prominent increases in both GM2 and GM3) was included as a reference. Quantitative analysis confirmed these observations. There was a 2.5-fold increase of GM3 (82 ± 20 nmol/g [n = 4] compared with a mean value of 34 nmol/g [n = 2] in controls) and of GM2 (70 ± 11 nmol/g, compared with a mean value of 29 nmol/g in the controls). The 2 controls included in this study fell well within the usual values established for Wt mice in our laboratory. The concentration of GD3 in *Mcoln1*$^{-/-}$ mice was marginally higher and that of GM1 marginally lower than those in Wt mice. Finally, there was no significant change in more complex gangliosides in the *Mcoln1*$^{-/-}$ mouse compared with Wt.

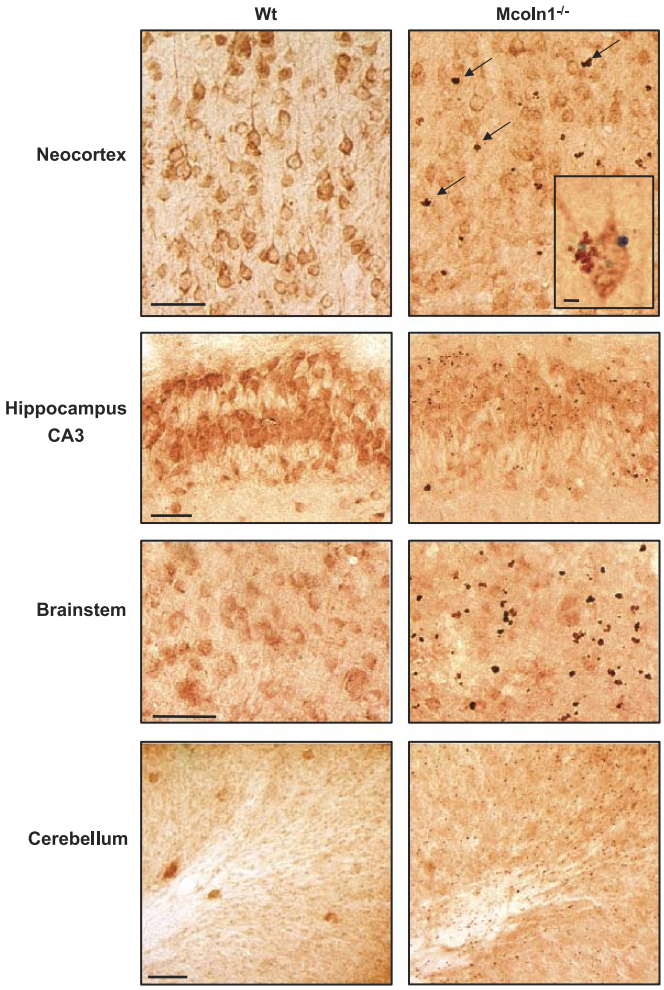

FIGURE 6. P62/SQSTM1 inclusions in the brain of *Mcoln1*$^{-/-}$ mice. Sections of a *Mcoln1*$^{-/-}$ mouse show large P62-positive inclusions in the neocortex and brainstem; no inclusions are seen in wild-type (Wt) mouse tissue. The inset in the top right panel shows a Nissl-counterstained section with P62 inclusions in a glial cell (identified based on size and morphology), directly adjacent to a cortical pyramidal neuron. In addition, smaller punctate inclusions are seen in pyramidal neurons of the CA3 region of the hippocampus; no inclusions are present in Wt mouse tissue. Finally, the granule cell layer of the cerebellum shows numerous small punctate inclusions, whereas the Wt mouse does not. Scale bars = (left panels) 50 μm and also pertain to matched right panels; inset scale bar = 5 μm.

Immunohistochemical Analysis of Ganglioside Accumulation in the *Mcoln1*$^{-/-}$ Mouse

In view of the suspected pathological prevalence of ganglioside accumulation in storage bodies from human MLIV disease (8–11) and our biochemical data suggesting increases in GM2, GM3, and possibly GD3 gangliosides in the *Mcoln1*$^{-/-}$ mice, immunohistochemical staining was performed in brain tissue of *Mcoln1*$^{-/-}$ mice. Immunoperoxidase labeling identified prominent GM2 ganglioside accumulation in neurons throughout cerebral hemisphere sections including the neocortex and hippocampus of the knockout mouse; Wt mouse tissue showed no GM2 staining (Figs. 2A, B). Higher magnification images showed GM2 to be prevalent primarily in perikarya of Nissl-counterstained cortical pyramidal neurons that were identified based on cell size and morphology in knockout but not Wt mice (Figs. 2C–F). Prominent GM2 accumulation was also found in brainstem regions of the *Mcoln1*$^{-/-}$ mouse (data not shown). In addition, cerebellar tissue showed occasional accumulation of GM2 in the granule cell layer, molecular layer, and Purkinje cell bodies of the *Mcoln*$^{-/-}$ mice, but this staining was much more sporadic and less prevalent compared with that in the cerebrum (Figs. 2G, H).

In contrast to GM2 accumulation, GM3 was found in a smaller subset of cortical pyramidal neurons specifically in the infragranular neocortex, the entorhinal cortex, and the CA3 region of the hippocampus, with no accumulation found in cerebellum or brainstem regions (Figs. 3A–D; data not shown). Similarly, GD3 ganglioside showed accumulation in cerebral hemisphere regions including the amygdala, the infragranular neocortex, the entorhinal cortex, and the CA1 and CA2 regions of the hippocampus (Figs. 3E–I). GD3 immunoreactivity was also not detected in cerebellum or brainstem regions of the *Mcoln1*$^{-/-}$ mouse (data not shown).

Finally, despite the fact that there was no significant change in GM1 ganglioside by biochemical analysis, we found evidence of subcellular alterations in GM1 localization in the *Mcoln1*$^{-/-}$ mouse brain by immunohistochemistry. We observed an apparent redistribution of GM1 in cortical pyramidal neurons of the knockout mouse that differed significantly from the pattern of GM1 staining associated in Wt mice (Figs. 3J–M). Taken together with the biochemical data, these results indicate that GM2, GM3, and GD3 ganglioside accumulation, along with alterations in GM1 ganglioside distribution, is a major feature of the neuropathology of the *Mcoln1*$^{-/-}$ mouse.

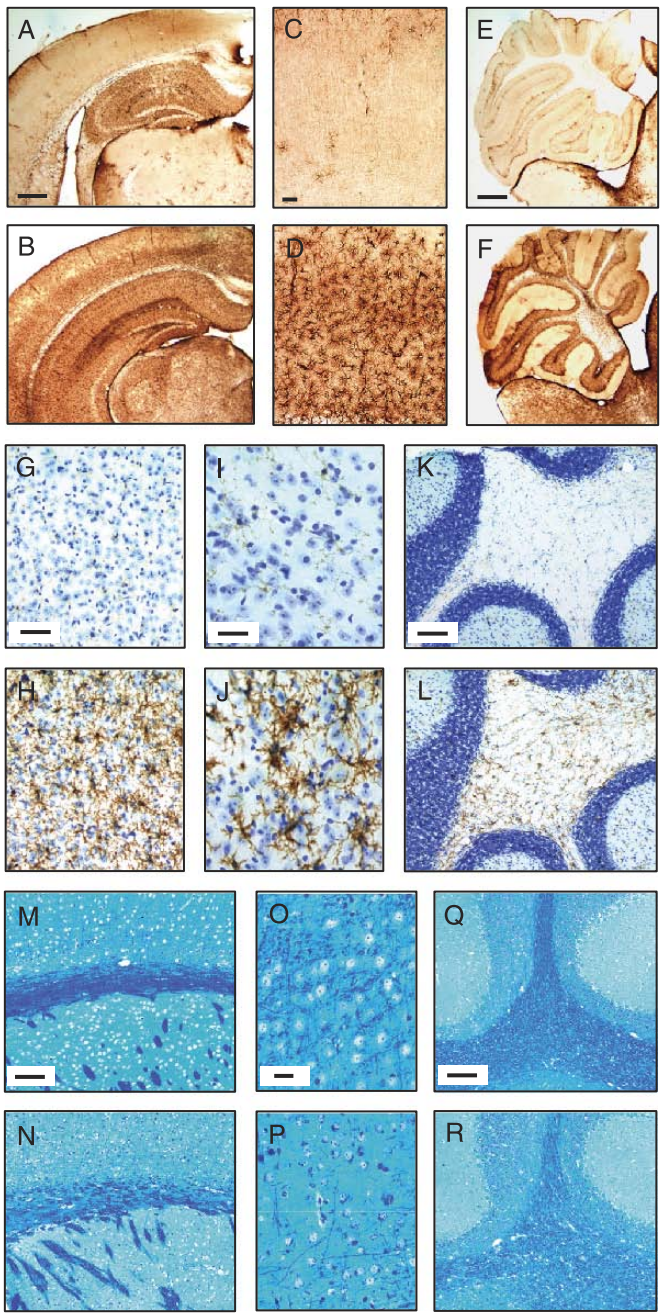

Cholesterol in the *Mcoln1*$^{-/-}$ Mouse

There have been conflicting reports on the presence of cholesterol accumulation in MLIV patient skin fibroblasts (19, 26). Although our HPTLC data indicated no change in total cholesterol levels, we evaluated tissue sections to determine whether or not cholesterol sequestration occurred in cells of the CNS of *Mcoln1*$^{-/-}$ mice by filipin labeling. In cerebral hemisphere sections of knockout mice, we found only sporadic focal accumulations of nonesterified cholesterol (i.e. up to approximately 5 μm in maximum diameter), which did not all seem to be perinuclear in location (Fig. 4A). In view of the well-documented abundance of nonesterified cholesterol found throughout the brain of NPC1 mice, sections from an NPC1 mouse were again used as a reference (Figs. 4A, B). In addition, cerebellar sections of *Mcoln1*$^{-/-}$ mice showed some filipin labeling in the Purkinje cell layer specifically in Purkinje cell apical dendrites, with less accumulation in the molecular layer (Fig. 4B). These results suggest that cholesterol sequestration in the CNS of the *Mcoln1*$^{-/-}$ mouse is not as conspicuous as it is in other lysosomal diseases including NPC1.

GM1, GM2, and LAMP2 Localization

Cortical sections were colabeled for GM1 and GM2, and for GM2 and LAMP2 and assessed by confocal immunofluorescence microscopy. GM1 and GM2 gangliosides showed almost no colocalization in individual cortical pyramidal neurons of the *Mcoln1*$^{-/-}$ mouse (Fig. 5A). Significant increases in LAMP2-positive vesicles were previously shown in the perikaryon of cortical pyramidal neurons of knockout compared with Wt mice by immunoperoxidase staining (21). In addition, given the prevalence of GM2 ganglioside storage throughout cortical pyramidal neurons by our immunohistochemical analysis, we anticipated that GM2 accumulation occurred in LAMP2-positive late endosomes/lysosomes. In

FIGURE 7. Glial involvement in the brains of *Mcoln1*$^{-/-}$ mice. **(A–F)** Brain sections labeled by immunoperoxidase for glial fibrillary acidic protein (GFAP) show weak reactivity in the wild-type (Wt) mouse **(A)**, but strong staining throughout the cortex of the *Mcoln1*$^{-/-}$ mouse **(B)**. Higher magnification images show GFAP staining in the neocortex of the Wt mouse **(C)** and the *Mcoln1*$^{-/-}$ mouse **(D)**. GFAP staining in the cerebellum of the Wt **(E)** and *Mcoln1*$^{-/-}$ mouse **(F)** shows a similar pattern. **(G–L)** Microglial staining for CD11b in Wt mouse neocortex shows weak reactivity **(G)** compared with the *Mcoln1*$^{-/-}$ mouse **(H)**. Similarly, there was weak staining in a Wt mouse brainstem **(I)** and white matter tracts of the cerebellum **(K)** compared with the strong immunoreactivity in brainstem **(J)** and cerebellum **(L)** of the *Mcoln1*$^{-/-}$ mouse. **(M–R)** Luxol fast blue staining of paraffin-embedded tissue identified decreased myelination as indicated by less intense blue staining of the subcortical white matter of the *Mcoln1*$^{-/-}$ mouse **(N)** compared with a Wt mouse **(M)**. There is less staining in sections of deep layer cortex and white matter tracts of the cerebellum of the *Mcoln1*$^{-/-}$ mouse **(P, R)** compared with a Wt mouse **(O, Q)**. Scale bars = **(A** and **E)** 500 μm and also pertain to **B** and **F**, respectively; **(C** and **G)** 50 μm and pertain to **D** and **H**, respectively; **(I)** 25 μm and pertains to **J; (K**, **M**, and **Q)** 100 μm and pertain to **L**, **N**, and **R**, respectively; **(O)** 20 μm and pertains to **P**.

contrast to the GM1 and GM2 double labeling, LAMP2 and GM2 immunofluorescence staining showed prominent colocalization in cortical pyramidal neurons (Fig. 5B). We did, however, observe some GM2 accumulation independent of LAMP2 staining indicating that GM2 sequestration is not completely confined to LAMP2-positive compartments.

P62/SQSTM1 Accumulation in Brain of the *Mcoln1*$^{-/-}$ Mouse

P62/SQSTM1 is an LC3- and ubiquitin-binding protein believed to play a role in the targeting of ubiquitinated proteins for lysosomal degradation through the macroautophagy pathway (27–29). Recent evidence has suggested that MLIV disease patient fibroblasts show alterations in macroautophagy, specifically an induction in autophagosome formation and inefficiency in autophagosome/lysosome fusion events (30). Furthermore, P62 was found to accumulate in these fibroblasts as protein inclusions, likely resulting from deficiencies in protein degradation and possible alterations in macroautophagy (30). Therefore, we evaluated the presence of P62 in the brains of *Mcoln1*$^{-/-}$ mice by immunoperoxidase labeling and found inclusions throughout cortical and cerebellar brain regions, including the neocortex, hippocampus, brainstem, and granule cell layer of the cerebellum (Fig. 6). These inclusions were large in neocortex and brainstem (i.e. up to 5 μm) and seemed to be present in the neuropil, as well as in cell bodies including glial cells characterized as such by their size and morphology (Fig. 6, inset). In contrast, P62 inclusions in the hippocampus and cerebellum were much smaller and occurred in a more punctate pattern in the pyramidal neuron and granule cell layers, respectively. Purkinje cells did not exhibit P62-positive inclusions. These results indicate that P62 pathology is present in the CNS, suggesting that protein degradation is compromised and that there may be alterations in macroautophagy in the brains of *Mcoln1*$^{-/-}$ mice.

Glial Cell Activation and Reduced Myelination in the Mcoln1$^{-/-}$ Mouse

Immunoperoxidase staining for GFAP was performed on brain tissue; these preparations showed increased immunostaining in cerebral sections of *Mcoln1*$^{-/-}$ compared with WT mice (Figs. 7A–D). There was also marked upregulation of GFAP in the cerebellum and brainstem regions particularly in the granule cell layer and white matter tracts (Figs. 7E, F). In addition, an immunostaining for the microglia marker CD11b demonstrated a similar pattern of strong immunoreactivity in *Mcoln1*$^{-/-}$ mouse brain sections. Specifically, there were increases in immunoreactivity of microglia in neocortical regions (Figs. 7G, H), brainstem regions (Figs. 7I, J), and white matter tracts of the cerebellum (Figs. 7K, L). These results suggest the presence of reactive astrocytes and microglial activation throughout the CNS of end-stage *Mcoln1*$^{-/-}$ mice.

In view of the biochemical analysis showing a slight decrease in the myelin-associated lipid galactosylceramide, Luxol fast blue staining was performed on paraffin-embedded *Mcoln1*$^{-/-}$ tissue to assess alterations in myelination. A slight decrease in staining for myelin compared with Wt mice was observed in the corpus callosum, deep layer neocortex, and cerebellar white matter tracts (Figs. 7M–R).

Autofluorescent Material in the Absence of Subunit C of Mitochondrial ATP Synthase

Accumulation of autofluorescent material in skin fibroblasts as well as in brain tissue has been described previously as a hallmark of MLIV disease (9, 31, 32). Analysis of brain tissue from *Mcoln1*$^{-/-}$ mice showed an abundance of autofluorescent material throughout the CNS that was detectable both with 488- and 543-nm excitation and over a wide range of emission wavelengths from 511 to 700 nm. Autofluorescent material primarily accumulated in a perinuclear punctate pattern in neurons of the neocortex and hippocampus (Fig. 8). In addition, autofluorescence was evident throughout the cerebellum and brainstem regions of the *Mcoln1*$^{-/-}$ mouse (Fig. 8 and data not shown). In cerebellum, autofluorescent material was found primarily in the Purkinje cell layer including accumulation in Purkinje cell bodies, whereas smaller puncta were evident throughout the molecular and granule cell layers.

Storage of autofluorescent material is a common neuropathological hallmark of another group of lysosomal diseases collectively known as the neuronal ceroid lipofuscinoses (NCL). In addition to this autofluorescent storage material, most forms of NCL show accumulations of the SCMAS (33). We performed an immunohistochemical stain for SCMAS in the *Mcoln1*$^{-/-}$ mouse but found no detectable accumulation in cerebrum or cerebellum (data not shown).

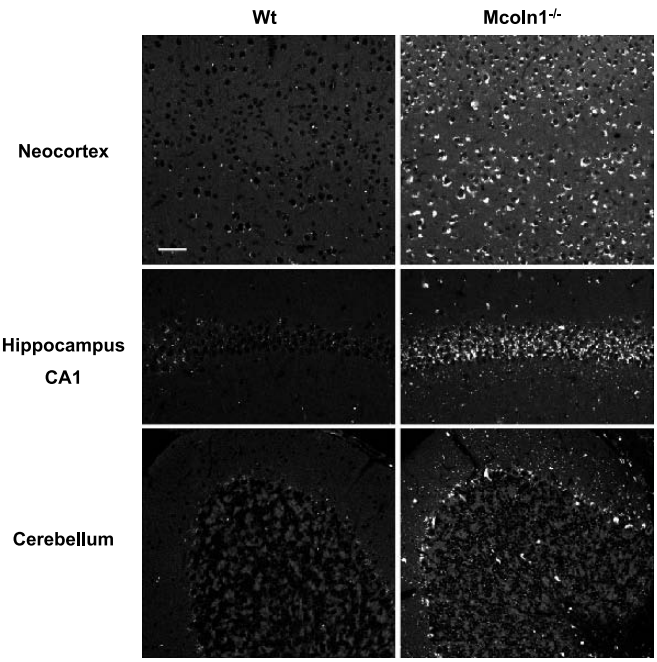

FIGURE 8. Accumulation of autofluorescent material throughout the CNS of a *Mcoln1*$^{-/-}$ mouse. Large amounts of autofluorescence are evident in cell bodies of the neocortex, the CA1 region of the hippocampus, and the cerebellum of a *Mcoln1*$^{-/-}$ mouse compared with a Wt mouse. Scale bar = 50 μm and pertains to all panels.

Axonal Spheroids

Axonal dystrophy in the form of axonal spheroids is a common neuropathological hallmark of lysosomal diseases including NPC1. Axonal spheroids are characterized morphologically as abnormal focal swellings composed of aggregated material along myelinated and unmyelinated axons that may cause and/or result from defects in axonal transport (33).

We found large numbers of axonal spheroids in the cerebellum in *Mcoln1*$^{-/-}$ mice. The spheroids were detected throughout Purkinje cell axons and cerebellar white matter tracts by calbindin D-28K immunoperoxidase staining (Figs. 9A, B). By EM, we found cross-sections of large myelinated Purkinje cell axons containing multivesicular and dense bodies along with an abundance of mitochondria (Figs. 9C, D). The accumulated material in axonal spheroids of the knockout mouse was distinctly different in appearance and size from the granulomembranous storage bodies found in the perikarya of cortical pyramidal neurons (Fig. 9E) previously described in human patients and mice (9, 21). Specifically, the multivesicular and dense bodies were typical of spheroids in other lysosomal diseases; that is, they varied in size from approximately 0.1 to 0.5 μm, whereas the storage bodies in neuronal perikaryon appeared more amorphous in shape and were as large as 1 μm.

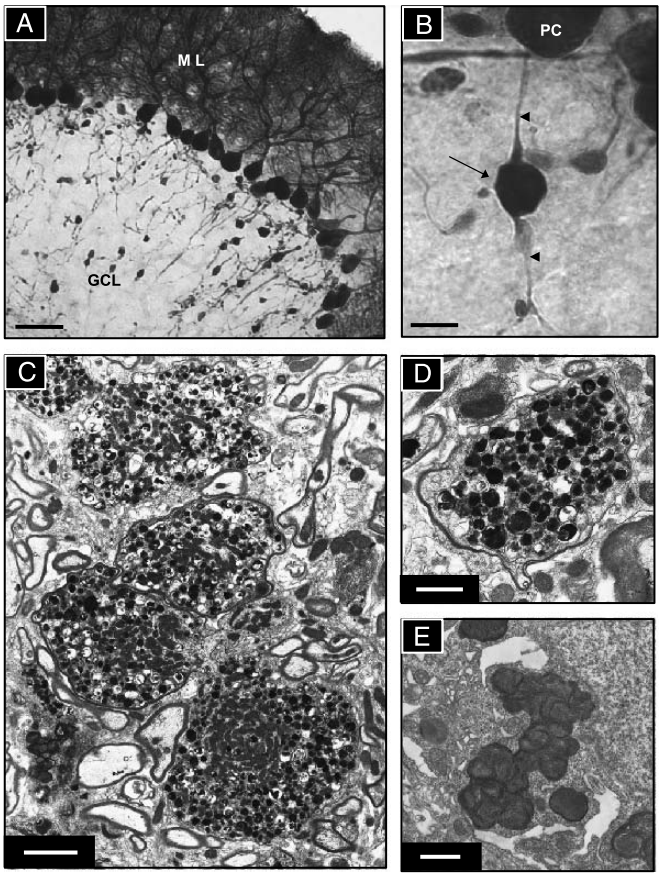

FIGURE 9. Axonal spheroids in the cerebellum of the *Mcoln1*$^{-/-}$ mouse. **(A, B)** Calbindin immunoperoxidase labeling demonstrates a large number of axonal spheroids in Purkinje cell axons in a *Mcoln1*$^{-/-}$ mouse (ML, molecular layer; GCL, granule cell layer). Higher magnification **(B)** of an axonal spheroid extending from a Purkinje cell is calbindin-positive (arrow indicates spheroid; arrowheads show proximal and distal portions of the axon in relation to the spheroid and Purkinje cell body; PC, Purkinje cell). **(C, D)** Electron microscopy of axonal spheroids in myelinated axons of cerebellum. There is accumulation of multivesicular and dense bodies and large numbers of mitochondria **(C, D)** and granulomembranous storage bodies in the perikaryon of a cortical pyramidal neuron **(E)**. Scale bars = **(A)** 50 μm; **(B)** 10 μm; **(C)** 2 μm; **(D** and **E)** 1 μm.

DISCUSSION

This is the first neuropathological characterization of the end-stage *Mcoln1*$^{-/-}$ mouse model. We document ganglioside accumulation, along with the presence of P62/SQSTM1 inclusions, glial cell activation and reduced myelination, the accumulation of autofluorescent material, and an abundance of axonal spheroids as major neuropathological features of the *Mcoln1*$^{-/-}$ mouse.

Interestingly, our biochemical analysis of cerebrum from the *Mcoln1*$^{-/-}$ mouse identified a small but significant increase in the phospholipid BMP that is found in multivesicular late-endosomal and lysosomal internal membranes (25). In human patients, a slight increase of BMP in brain tissue has been found in some lysosomal diseases such as infantile NCL disease (CLN1) (34, 35), but not in others, including Niemann-Pick disease A in which this lipid is strikingly increased in liver and spleen. The largest increase of BMP in brain tissue reported to date has been in the cathepsin D knockout mouse model of CLN10 disease (23). It should be noted that few mouse models of lysosomal diseases have been investigated with regard to this lipid, and at present, the significance of this finding remains unclear.

Aberrant elevations and accumulation of gangliosides (including increases in GD3 and GM3 gangliosides) have been documented in MLIV patient skin fibroblasts (8). In addition, in the CNS, gangliosides (specifically GM1 and GM2) have been shown to increase 50% in gray matter and 3-fold in white matter based on a brain biopsy analysis (9). These 2 studies are conspicuously at odds with the only autopsy report of an MLIV patient that found no significant neuronal accumulation of polar lipids such as gangliosides or phospholipids (36). The discrepancies between these studies address the complexity and heterogeneity of clinical and pathological manifestations associated with different mutations in *MCOLN1* (37). Our data suggest that the *Mcoln1*$^{-/-}$ knockout mouse model displays considerable neuropathological ganglioside accumulation, including increases in GM2, GM3, and GD3 gangliosides.

In addition, although GM1 ganglioside levels were not elevated in the *Mcoln1*$^{-/-}$ mouse by biochemical analysis, we did observe some alterations in the distribution of GM1 as indicated by changes in the immunostaining pattern compared with Wt mice. This alteration may indicate slower processing of GM1 ganglioside through the endocytic pathway; this supports previous observations describing membrane trafficking defects associated with TRP-ML1 loss of function in MLIV disease (14–17).

We found by immunofluorescence confocal microscopy that GM1 and GM2 did not colocalize in individual cortical pyramidal neurons of the *Mcoln1*$^{-/-}$ mouse, indicating that these gangliosides are present in different compartments. In addition, we found a large amount of vesicular GM2 ganglioside accumulation colocalizing with LAMP2 in individual neurons. We also found, however, several neurons in which GM2 clearly appeared to be independent of LAMP2 staining, suggesting that this sequestration may occur in a vesicle population other than late endosomes and lysosomes, (i.e. in early or recycling endosomal compartments, along a ganglioside salvage pathway including the trans-Golgi Network (TGN), and/or along a de novo synthesis pathway).

P62/SQSTM1 has been shown to aggregate as a major component of protein inclusion bodies in several neurodegenerative diseases (27, 38–41). In addition, P62 accumulation in brain tissue has been found in mouse lysosomal disease models including multiple sulfatase deficiency and mucopolysaccharidosis type IIIA in which autophagosome maturation is believed to be compromised secondary to storage in dysfunctional lysosomes (42). In MLIV disease fibroblasts, previous studies have shown the accumulation of fragmented mitochondria (43), an induction in autophagosome formation, inefficient autophagosome/lysosome fusion, and P62 accumulation (30). Taken together, these studies suggest that P62 accumulation results from deficiencies in protein degradation. The relationship of P62 to altered macroautophagy and the pathogenetic consequences of this feature are not completely clear.

In view of our current findings of the presence of P62 inclusions in the CNS of the *Mcoln1*$^{-/-}$ mouse, we speculate that this pathology indicates dysfunctional protein degradation and possible altered macroautophagic function. We propose that evidence of an induction in autophagosome formation in MLIV disease fibroblasts (30) may result from a "housekeeping" response in which autophagosomes engulf storage bodies in an effort to clear this material from the cell. Similarly, macroautophagy induction may be a more general response to a condition of starvation. Specifically, ganglioside storage resulting from inefficiently trafficked material may deprive cells of critical molecular components generated during substrate degradation in lysosomes. It is possible that macroautophagy may be subsequently upregulated as a "self-eating" mechanism in an attempt to generate these components for reutilization in a salvage pathway within the cell. In view of evidence of the inefficiency in autophagosome maturation in MLIV (30), however, this upregulation may be futile and detrimental because overactive autophagy has been associated with type II (autophagic) cell death (44). Further investigating the role of autophagy in the CNS of the *Mcoln1*$^{-/-}$ mouse will likely prove critical in elucidating the pathogenic cascades associated with MLIV disease.

Previous studies have shown an accumulation of autofluorescent material in skin fibroblasts of MLIV patients (31, 32). In addition, analysis of an MLIV patient brain biopsy showed accumulation of dense autofluorescent material consistent with the lipopigments ceroid and lipofuscin (9). In contrast, however, one autopsy report of an MLIV patient identified no significant autofluorescence in neurons (36), again indicating the complexity of the clinical and pathological consequences associated with specific mutations in the *MCOLN1* gene (37). The autofluorescent material found in the *Mcoln1*$^{-/-}$ mouse showed a relatively large band of emission both with 488- and 543-nm excitation, in part overlapping with that observed in a mouse model of late-infantile neuronal ceroid lipofuscinosis (CLN2 disease) (45). Accumulation of autofluorescent material in the *Mcoln1*$^{-/-}$ mouse did not, however, seem to be attributable to SCMAS, which commonly accumulates in NCL diseases, because it was not detectable by immunohistochemistry in the present study.

Axonal spheroids are characterized by the accumulation of aggregated multivesicular and dense bodies, tubulovesicular profiles, and mitochondria affecting axonal transport (33). Purkinje cells are particularly susceptible to axonal spheroid pathology and the incidence of axonal spheroids in GABAergic neurons correlates closely with the clinical severity (46). At least one study of a brain biopsy from an MLIV patient reported swollen axons filled with dense and multivesicular bodies (9). In addition, neuroaxonal damage analyzed by proton magnetic resonance spectroscopic imaging was found to be common in a study of 14 MLIV disease patients (47).

In lysosomal diseases, accumulated material in axonal spheroids is usually different from the primary storage material predominately observed in neuronal cell bodies (48). In the *Mcoln1*$^{-/-}$ mouse, the material accumulated in spheroids was morphologically distinct from the storage bodies in neuronal perikarya that was previously reported (21). Motor pathways seem to be impaired much more severely than sensory pathways in the CNS of MLIV patients (47). This observation is significant for linking the abundance of axonal spheroid pathology in the cerebellum of the *Mcoln1*$^{-/-}$ mouse with the clinical phenotype associated with motor dysfunction in MLIV.

In summary, although MLIV disease presents clinically with a wide spectrum of manifestations, the complex neurological components of the disease are particularly debilitating and severe. Our characterization of the *Mcoln1*$^{-/-}$ mouse has further established the involvement of the brain in MLIV. We have identified the major neuropathological components of the mouse model in an effort to better understand TRPML1 function and the pathogenic cascades in MLIV disease.

ACKNOWLEDGMENTS

The authors thank Nafeeza Ali for the filipin labeling and microglial staining experiments and Orane Gillet for the ganglioside biochemical analysis.

REFERENCES

1. Bargal R, Avidan N, Ben-Asher E, et al. Identification of the gene causing mucolipidosis type IV. Nat Genet 2000;26:118–23
2. Sun M, Goldin E, Stahl S, et al. Mucolipidosis type IV is caused by mutations in a gene encoding a novel transient receptor potential channel. Hum Mol Genet 2000;9:2471–78
3. Zeevi DA, Frumkin A, Bach G. TRPML and lysosomal function. Biochim Biophys Acta 2007;1772:851–58
4. Berman ER, Livni N, Shapira E, et al. Congenital cornea clouding with abnormal systemic storage bodies: A new variant of Mucolipidosis. J Pediatr 1974;84:519–26

5. Chitayat D, Meunier CM, Hodgkinson KA, et al. Mucolipidosis type IV: Clinical manifestations and natural history. Am J Med Genet 1991;41: 313–18
6. Reis S, Sheffer RN, Merin S, et al. Mucolipidosis type IV: A mild form with late onset. Am J Med Genet 1993;47:392–94
7. Altarescu G, Sun M, Moore DF, et al. The neurogenetics of mucolipidosis type IV. Neurology 2002;59:306–13
8. Bach G, Cohen MM, Kohn G. Abnormal ganglioside accumulation in cultured fibroblasts from patients with mucolipidosis IV. Biochem Biophys Res Commun 1975;66:1483–90
9. Tellez-Nagel I, Rapin I, Iwamoto T, et al. Mucolipidosis IV. Clinical, ultrastructural, histochemical, and chemical studies of a case, including a brain biopsy. Arch Neurol 1976;33:828–35
10. Bargal R, Bach G. Phospholipids accumulation in mucolipidosis IV cultured fibroblasts. J Inherit Metab Dis 1988;11:144–50
11. Bargal R, Bach G. Mucolipidosis type IV: Abnormal transport of lipids to lysosomes. J Inherit Metab Dis 1997;20:625–32
12. Raychowdhury MK, González-Perrett S, Montalbetti N, et al. Molecular pathophysiology of mucolipidosis type IV: pH dysregulation of the mucolipin-1 cation channel. Hum Mol Genet 2004;13:617–27
13. Cantiello HF, Montalbetti N, Goldmann WH, et al. Cation channel activity of mucolipin-1: The effect of calcium. Pflugers Arch 2005;451: 304–12
14. LaPlante JM, Ye CP, Quinn SJ, et al. Functional links between mucolipin-1 and Ca^{2+}-dependent membrane trafficking in mucolipidosis IV. Biochem Biophys Res Commun 2004;322:1384–91
15. Luzio JP, Pryor PR, Bright NA. Lysosomes: Fusion and function. Nat Rev Mol Cell Biol 2007;8:622–32
16. Piper RC, Luzio JP. CUPpling calcium to lysosomal biogenesis. Trends Cell Biol 2004;14:471–73
17. Treusch S, Knuth S, Slaugenhaupt SA, et al. *Caenorhabditis elegans* functional orthologue of human protein h-mucolipin-1 is required for lysosome biogenesis. Proc Natl Acad Sci U S A 2004;101:4483–88
18. Bach G, Chen CS, Pagano RE. Elevated lysosomal pH in mucolipidosis type IV cells. Clin Chim Acta 1999;280:173–79
19. Soyombo AA, Tjon-Kon-Sang S, Rbaibi Y, et al. TRP-ML1 regulates lysosomal pH and acidic lysosomal lipid hydrolytic activity. J Biol Chem 2006;281:7294–301
20. Miedel MT, Rbaibi Y, Guerriero CJ, et al. Membrane traffic and turnover in TRP-ML1-deficient cells: a revised model for mucolipidosis type IV pathogenesis. J Exp Med 2008;205:1477–90
21. Venugopal B, Browning MF, Curcio-Morelli C, et al. Neurologic, gastric, and opthalmologic pathologies in a murine model of mucolipidosis type IV. Am J Hum Genet 2007;81:1070–83
22. Fujita N, Suzuki K, Vanier MT, et al. Targeted disruption of the mouse sphingolipid activator protein gene: A complex phenotype, including severe leukodystrophy and wide-spread storage of multiple sphingolipids. Hum Mol Genet 1996;5:711–25
23. Jabs S, Quitsch A, Käkelä R, et al. Accumulation of bis(monoacylglycero)phosphate and gangliosides in mouse models of neuronal ceroid lipofuscinosis. J Neurochem 2008;106:1415–25
24. McGlynn R, Dobrenis K, Walkley SU. Differential subcellular localization of cholesterol, gangliosides, and glycosaminoglycans in murine models of mucopolysaccharide storage disorders. J Comp Neurol 2004; 480:415–26
25. Kobayashi T, Beuchat MH, Lindsay M, et al. Late endosomal membranes rich in lysobisphosphatidic acid regulate cholesterol transport. Nat Cell Biol 1999;1:113–18
26. Pryor PR, Reimann F, Gribble FM, et al. Mucolipin-1 is a lysosomal membrane protein required for intracellular lactosylceramide traffic. Traffic 2006;7:1388–98
27. Bjørkøy G, Lamark T, Brech A, et al. P62/SQSTM1 forms protein aggregates degraded by autophagy and has a protective effect on Huntingtin-induced cell death. J Cell Biol 2005;171:603–14
28. Pankiv S, Clausen TH, Lamark T, et al. P62/SQSTM1 binds directly to Atg8/LC3 to facilitate degradation of ubiquitinated protein aggregates by autophagy. J Biol Chem 2007;282:24131–45
29. Shvets E, Fass E, Scherz-Shouval R, et al. The N-terminus and Phe52 residue of LC3 recruit p62/SQSTM1 into autophagosomes. J Cell Sci 2008;121:2685–95
30. Vergarajauregui S, Connelly PS, Daniels MP, et al. Autophagic dysfunction in mucolipidosis type IV patients. Hum Mol Genet 2008;17: 2723–37
31. Goldin E, Blanchette-Mackie EJ, Dwyer NK, et al. Cultured skin fibroblasts derived from patients with mucolipidosis 4 are auto-fluorescent. Pediatr Res 1995;37:687–92
32. Goldin E, Cooney A, Kaneski CR, et al. Mucolipidosis IV consists of one complementation group. Proc Natl Acad Sci U S A 1999;96:8562–66
33. Walkley SU. Pathogenic cascades and brain dysfunction. In: Platt FM, and Walkley SU, eds. Lysosomal Disorders of the Brain. New York, NY: Oxford University Press, 2004:290–324
34. Kahma K, Brotherus J, Haltia M, et al. Low and moderate concentrations of lysobisphosphatidic acid in brain and liver of patients affected by some storage diseases. Lipids 1976;11:539–44
35. Käkelä R, Somerharju P, Tyynelä J. Analysis of phospholipid molecular species in brains from patients with infantile and juvenile neuronal-ceroid lipofuscinosis using liquid chromatography-electrospray ionization mass spectrometry. J Neurochem 2003;84:1051–65
36. Folkerth RD, Alroy J, Lomakina I, et al. Mucolipidosis IV: Morphology and histochemistry of an autopsy case. J Neuropathol Exp Neurol 1995; 54:154–64
37. Goldin E, Caruso RC, Benko W, et al. Isolated ocular disease is associated with decreased mucolipin-1 channel conductance. Invest Ophthalmol Vis Sci 2008;49:3134–42
38. Kuusisto E, Salminen A, Alafuzoff I. Ubiquitin-binding protein p62 is present in neuronal and glial inclusions in human tauopathies and synucleinopathies. Neuroreport 2001;12:2085–90
39. Kuusisto E, Parkkinen L, Alafuzoff I. Morphogenesis of Lewy bodies: dissimilar incorporation of alpha-synuclein, ubiquitin, and p62. J Neuropathol Exp Neurol 2003;62:1241–53
40. Wooten MW, Hu X, Babu JR, et al. Signaling, polyubiquitination, trafficking, and inclusions: Sequestosome 1/p62's role in neurodegenerative disease. J Biomed Biotechnol 2006;2006:62079
41. King A, Al-Sarraj S, Shaw C. Frontotemporal lobar degeneration with ubiquitinated tau-negative inclusions and additional alpha-synuclein pathology but also unusual cerebellar ubiquitinated p62-positive, TDP-43-negative inclusions [published online ahead of print 2008]. Neuropathology
42. Settembre C, Fraldi A, Jahreiss L, et al. A block of autophagy in lysosomal storage disorders. Hum Mol Genet 2008;17:119–29
43. Jennings JJ, Zhu JH, Rbaibi Y, et al. Mitochondrial aberrations in mucolipidosis Type IV. J Biol Chem 2004;281:39041–50
44. Levine B, Kroemer G. Autophagy in the pathogenesis of disease. Cell 2008;132:27–42
45. Sleat DE, El-Banna M, Sohar I, et al. Residual levels of tripeptidyl--peptidase I activity dramatically ameliorate disease in late-infantile neuronal ceroid lipofuscinosis. Mol Genet Metab 2008;94:222–33
46. Walkley SU. Cellular pathology of lysosomal storage diseases. Brain Pathol 1998;8:175–93
47. Bonavita S, Virta A, Jeffries N, et al. Diffuse neuroaxonal involvement in mucolipidosis IV as assessed by proton magnetic resonance spectroscopic imaging. J Child Neurol 2003;18:443–49
48. Walkley SU. Pathobiology of neuronal storage disease. Int Rev Neurobiol 1988;29:191–244

